Cell Reports

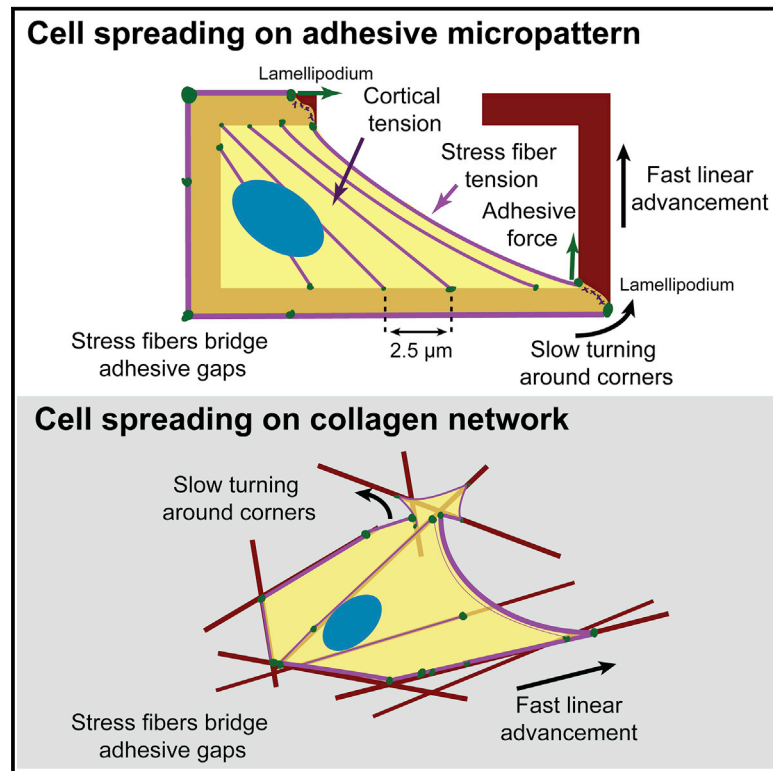# Extracellular Matrix Geometry and Initial Adhesive Position Determine Stress Fiber Network Organization during Cell Spreading

Graphical Abstract

Authors

Elena Kassianidou, Dimitri Probst,
Julia Jäger, Stacey Lee,
Anne-Lou Roguet,
Ulrich Sebastian Schwarz, Sanjay Kumar

Correspondence

schwarz@thphys.uni-heidelberg.de
(U.S.S.),
skumar@berkeley.edu (S.K.)

In Brief

Kassianidou et al. use adhesive micropatterns to recapitulate features of 3D extracellular matrices and to integrate live-cell imaging with mathematical modeling. They find that spreading trajectories are determined by a balance between adhesion energy, surface tension, and line tension, and that cells produce a stress fiber network that encodes the spreading history.

Highlights

- Spreading trajectories depend strongly on initial adhesive positions

- Cells bridge non-adhesive regions with an invaginated actin arc that drives spreading

- Stress fibers are generated in a periodic manner behind the advancing front

- The stress fiber network retains a spreading memory for ~50 min

CellPress

Extracellular Matrix Geometry and Initial Adhesive Position Determine Stress Fiber Network Organization during Cell Spreading

Elena Kassianidou,[1,2,6] Dimitri Probst,[3,6] Julia Jäger,[3,6] Stacey Lee,[1,2] Anne-Lou Roguet,[1,4] Ulrich Sebastian Schwarz,[3,*] and Sanjay Kumar[1,2,5,7,*]
[1]Department of Bioengineering, University of California, Berkeley, CA 94720-1762, USA
[2]UC Berkeley-UCSF Graduate Program in Bioengineering, University of California, Berkeley, Berkeley, CA 94720-1762, USA
[3]Heidelberg University, Institute for Theoretical Physics and BioQuant-Center for Quantitative Biology, Philosophenweg 19, 69120 Heidelberg, Germany
[4]École Polytechnique, 91120 Palaiseau, France
[5]Department of Chemical and Biomolecular Engineering, University of California, Berkeley, Berkeley, CA 94720-1762, USA
[6]These authors contributed equally
[7]Lead Contact
*Correspondence: schwarz@thphys.uni-heidelberg.de (U.S.S.), skumar@berkeley.edu (S.K.)
https://doi.org/10.1016/j.celrep.2019.04.035

SUMMARY

Three-dimensional matrices often contain highly structured adhesive tracks that require cells to turn corners and bridge non-adhesive areas. Here, we investigate these complex processes using micro-patterned cell adhesive frames. Spreading kinetics on these matrices depend strongly on initial adhesive position and are predicted by a cellular Potts model (CPM), which reflects a balance between adhesion and intracellular tension. As cells spread, new stress fibers (SFs) assemble periodically and parallel to the leading edge, with spatial intervals of ~2.5 μm, temporal intervals of ~15 min, and characteristic lifetimes of ~50 min. By incorporating these rules into the CPM, we can successfully predict SF network architecture. Moreover, we observe broadly similar behavior when we culture cells on arrays of discrete collagen fibers. Our findings show that ECM geometry and initial cell position strongly determine cell spreading and that cells encode a memory of their spreading history through SF network organization.

INTRODUCTION

Cell migration is essential for many tissue-level processes, including development, wound healing, and cancer metastasis (Ridley et al., 2003). Productive migration requires the integration of several subcellular processes, particularly advancement of the cell front and retraction of the rear. Leading-edge advancement is governed by a mechanical balance between actin polymerization, membrane tension, and myosin-driven retrograde flow, whereas trailing-edge retraction requires strong contractile forces to detach existing adhesions. Both processes are strongly regulated and connected by actomyosin stress fibers (SFs), which are nucleated according to the location and architecture

of new adhesions at the cell front and produce the high forces needed to rupture old adhesions at the rear (Blanchoin et al., 2014). In this way, the actin cytoskeleton choreographs a highly dynamic interplay with the matrix involving continuous and spatially targeted creation and dissolution of adhesions (Schwarz and Gardel, 2012).

Cell spreading, the process through which newly attached cells encounter and engage the extracellular matrix (ECM), is a crucial prerequisite for cell migration and requires the coordination of the same subcellular processes. Investigation of the initiation and control of spreading has therefore yielded valuable insights into the fundamental principles of cell migration. The rate of spreading, final spreading area, and total traction force during spreading on 2D substrates coated evenly with ECM tend to increase with both ligand concentration and substrate stiffness (Engler et al., 2004; Reinhart-King et al., 2005; Nisenholz et al., 2014), with membrane tension constraining and potentially terminating lamellipodial protrusions (Raucher and Sheetz, 2000). While very high ligand concentration in 2D culture is known to decrease cell spreading (Palecek et al., 1997; Engler et al., 2004; Gupton and Waterman-Storer, 2006), this is not expected to be a major factor in 3D gels with sufficiently large mesh sizes for cell migration (Wolf et al., 2013). It has been observed that 2D cell spreading often occurs in a periodic manner (Giannone et al., 2004; Burnette et al., 2011), in good agreement with predictions from mathematical models suggesting that an actin-based gel pushing against a tensed membrane and flowing over mechanosensitive cell matrix adhesions can have oscillatory solutions with regard to protrusion velocity, the deposition of new adhesions, and the formation of new actin structures (Shemesh et al., 2009, 2012). A recent experimental study has identified the interplay between membrane tension and actin dynamics as a key regulator for the formation of new adhesion sites (Pontes et al., 2017). As the actin network polymerizes against the membrane, membrane tension rises and starts to feed back by compressing the lamellipodium. Nascent adhesions below the lamellipodium mature into focal adhesions (FAs) and prevent the lamellipodium from flowing backward, eventually leading to its

mechanical disintegration and allowing the cycle to begin again. This scenario also provides an explanation for the formation of transverse arc SFs behind the lamellipodium, namely through non-muscle myosin II-assisted (NMMII) assembly of actin filaments that originate from the disintegrating lamellipodium. These transverse arcs then flow retrograde and fuse into ventral SFs (Tojkander et al., 2015). A similar coordination of lamellipodial protrusion, membrane tension, and adhesion site formation has recently been described both experimentally and by a mathematical model for lateral waves during keratocyte migration (Barnhart et al., 2017). The spatial and temporal periodicity of the subcellular structures formed during cell spreading may also be related to recent findings describing the actin cytoskeleton as a locally excitable medium (Bement et al., 2015; Graessl et al., 2017), although in the context of cell spreading, membrane tension and global coordination can also play an important role (Diz-Muñoz et al., 2016).

While such studies have provided tremendous insight into the mechanisms of cell spreading, they have almost always been conducted on homogeneously coated, 2D ECM surfaces. This leads to spreading with a broad and convex lamellipodial front, which is constrained by ECM rigidity and adhesiveness but not by ECM spatial organization. Physiological matrices, however, are often highly structured and compel cells to spread along pre-defined ECM tracks (e.g., collagen fibers) and form SFs and lamellipodial structures that span non-adhesive regions, thus leading to stellate cell shapes and concave fronts (Cukierman et al., 2001; Grinnell and Petroll, 2010; Owen et al., 2017). In general, ECM structure is known to dictate the mode and kinetics of cell migration (Gardel et al., 2010; Doyle and Yamada, 2016). Understanding the biophysical and molecular parameters that control spatially restricted spreading would produce important new mechanistic insights into processes such as development, wound healing, and tumor invasion, all of which often proceed in highly structured matrix environments. For example, in tumor invasion through collagen-rich ECMs, leader cells often align collagen fibers, facilitating the invasion of subsequent follower cells (Wolf et al., 2007; Carey et al., 2013). Similarly, *Drosophila* embryonic rotation facilitates the deposition of an aligned, fibrillar ECM that guides subsequent cell migration and tissue assembly (Haigo and Bilder, 2011).

Adhesive micropatterns have emerged as a valuable paradigm for studying the effect of structured ECMs on cell processes in a standardized way that can be quantified and modeled (Théry, 2010; Albert and Schwarz, 2016b; Ruprecht et al., 2017). For example, adhesive micropatterns have been used to describe the formation of peripheral SFs in response to the geometry of the extracellular environment (Théry et al., 2006) and their retraction dynamics after laser cutting within SF networks (Kassianidou et al., 2017). We reasoned that such micropatterns could also be used to mimic some of the aspects of cell spreading in 3D structured environments (Doyle et al., 2009; Ramirez-San Juan et al., 2017). Earlier approaches of this kind have mainly focused on mimicking the 1-dimensional (1D) nature of cell migration along one fiber but have not addressed the effect of corners and concave fronts. A recent study using flower-shaped micropatterns has addressed how cells span concave regions but not how cells spread along fiber-like structures that are

typical of 3D ECM (Chen et al., 2019). Here, we use micropatterns to force a cell to spread along preexisting matrix geometries with corners while assembling SFs that span non-adhesive regions, thereby recapitulating several important features of migration in 3D fibrillar environments encountered *in vivo*. Our main focus is on the dynamic formation of the SF network in the spreading cell. We show that the spreading process in structured, micropatterned matrices is strongly guided by ECM geometry and initial cell positioning. More specifically, spreading along 1D legs of the patterns is characterized by the periodic formation of FAs and SFs, as has been observed for cells spreading on homogeneous matrices. By performing detailed comparisons between different types of micropatterns, we identify geometrical bottlenecks for cell spreading and adhesion, which dictate the location and timing of the SF assembly. Our observations of the organization of the SF network can be closely recapitulated with a relatively simple mathematical framework consisting of a cellular Potts model (CPM) for shape dynamics supplemented by the experimental observation that in our paradigm, new SFs are deposited with a typical distance along the 1D spreading trajectory. These observations and predictions are supported by the imaging of cells migrating on arrays of discrete collagen fibers. Our findings offer general regulatory principles that should be directly applicable to understanding and controlling cell spreading in fully 3D environments.

RESULTS

Cell Spreading Rate Depends on Pattern Geometry and Initial Adhesive Position

To investigate cell spreading in standardized ECM geometries, we designed 2 rectangular patterns of aspect ratio 1.9 (48 × 25 μm) with a 15-μm gap located at either the top ("top pattern," Figure 1A) or the side of the pattern ("side pattern," Figure 1B), which were coated with fibronectin (FN). We then seeded U2OS red fluorescent protein (RFP)-LifeAct cells and conducted time-lapse epifluorescence imaging to visualize the actin dynamics during cell spreading. It has previously been shown that after sedimentation from solution, cell binding to an adhesive substrate is a random and spatially uniform process (Röttgermann et al., 2014). However, a micropattern breaks this symmetry and offers the opportunity to ask how initial adhesive position influences spreading kinetics. The cells seeded exhibited 3 possible initial attachment positions for each pattern. For the top pattern, cells attached to either the short edge of the pattern (left or right; treated as identical due to vertical symmetry) or the long edge (Figure 1A). For the side pattern, cells adhered to the left short edge or at either the top or bottom long edge (treated as identical due to horizontal symmetry) (Figure 1B). As cells adhered, they initiated spreading along the FN-coated lines, analogous to 1D spreading along a stripe (Doyle et al., 2009). As cells encountered a corner, they turned and spanned the non-adhesive region in the center of the pattern using a peripheral SF. As expected, this spanning started much earlier for cells that attached to the short sides than to the long sides, with cells adherent to short sides already forming bridges by the first time point of observation (Figures 1A and 1B, left columns). As spreading progressed, cells deposited many internal
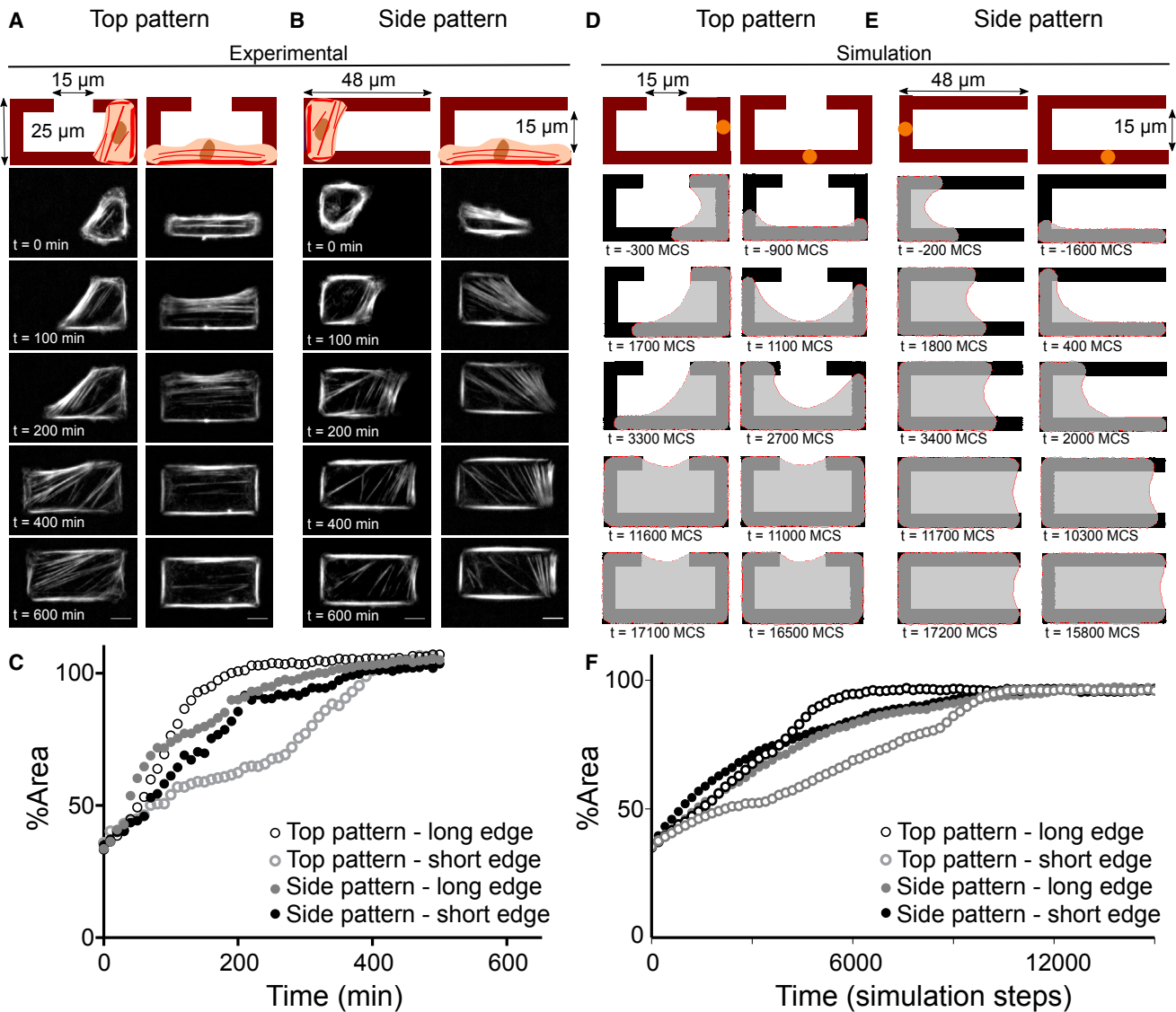
Figure 1. Spreading Kinetics Depend on Pattern Geometry and Initial Cellular Adhesive Position
(A and B) Schematic of (A) top pattern and (B) side pattern, where dark red represents the region where FN is present. Shown below are representative images of U2OS RFP-LifeAct cells spreading on each pattern initially adhering to either the short edge (left) or long edge (right) of each pattern at different time points (Video S1).
(C) Spreading kinetics for cells shown in (A) and (B), expressed as the percentage of the final area at each time point.
(D and E) CPM simulation of a cell adhered to and spread on (D) top pattern or (E) side pattern (Video S2).
(F) Simulations of cell area over time as cells adhere to and spread on each pattern. Scale bars, 10 μm.
See also Figures S1 and S2.

SFs that bridged the legs of the pattern. After the completion of spreading, each cell covered the whole pattern, with 1 peripheral SF located at the position of the adhesive gap and a network of internal SFs dispersed throughout the cell. Using differential interference contrast (DIC) and epifluorescence microscopy, we observed that during spreading, cells formed 2 lamellipodia, 1 at each end of the peripheral SF spanning from one side of the pattern to the other (Figure S1, circled regions). In contrast to the broad lamellipodium that is typically encountered during cell spreading on homogeneously coated sub-

strates, these lamellipodia were locally restricted and reminiscent of those encountered during spreading along single fibers in 3D ECM (Doyle et al., 2015; Doyle and Yamada, 2016).

We next quantified area changes over time for each pattern geometry and initial position (Figures 1C and S2). The spreading area of both individual cells (Figure 1C) and averages of many cells (Figure S2A) followed a hyperbolic curve, as previously observed (Reinhart-King et al., 2005). We then fitted individual cell trajectories and extracted exponential time constants (Figure S2C). Cells that adhered to the short edges of the top pattern

exhibited a statistically larger time constant than cells that adhered to the long edge (Figures 1C, black versus gray empty circles, and S2C; Video S1, A and B). This shows that the spreading path is dictated by the initial adhesive position and strongly influences the rate of cell spreading. Specifically, cells that attached to the short edge of the top pattern were forced to rotate and bridge the long diagonal of the pattern (Figures 1A and 1B, images at 200 min), whereas cells that attached to the long edge of the top pattern did not go through this diagonal configuration. In contrast, cells that attached to the long edges of the side pattern exhibited statistically indistinguishable spreading kinetics from cells that attached to the short edge of the side pattern (Figures 1C, black versus gray filled circles, and S2C; Video S1, C and D). Our results suggest that constraints on spreading trajectories imposed by ECM geometry strongly influence the spreading process, especially if it involves turning corners and bridging long distances.

Cell Spreading Trajectories and Spreading Rates Are Predicted by a CPM

To understand the biophysical mechanisms that underlie the experimentally observed spreading dynamics, we used our previously published 2D CPM (Albert and Schwarz, 2014, 2016a) to simulate cell spreading on patterns (Figures 1D–1F; Video S2). We modeled cells at the initial point of adhesion as ellipses with a minor axis of 5 μm and a major axis such that they cover the corresponding edge of the pattern to mimic experimental observations. We first needed to determine CPM parameters, which are specific to each cell-matrix context (Albert and Schwarz, 2016a). One important CPM parameter is the adhesion strength, which governs the ability of cells to spread on the micropatterns, and was chosen to be just strong enough to allow spreading (W = 10 nN/μm). Cell shape during spreading is determined by a balance between this adhesive energy and the surface tension, the simple line tension, and the elastic line tension (Bischofs et al., 2008; Albert and Schwarz, 2014, 2016a, 2016b; Brand et al., 2017). The surface tension represents cortical contractility over the whole surface and was previously estimated to be approximately σ = 0.7 mN/m for keratinocytes (Mertz et al., 2012). The simple line tension represents the tension along the cell periphery and, similar to the surface tension, is expected to be generated primarily by NMMII motors. The simple line tension is also the main determinant of traction force at FAs pinning the contour of strongly adhesive cells between inward curved peripheral SFs, which typically is on the order of a few nanonewtons (Bischofs et al., 2009). For these simulations, we chose the simple line tension as λ_s = 7 nN. The elastic line tension represents additional forces in the cell periphery generated by actin cross-linkers such as α-actinin that are stretched in peripheral SFs. The corresponding elastic modulus is estimated by applying the tension-elasticity model (Bischofs et al., 2008) (see STAR Methods for more detail), which recently has been confirmed for cells in 3D scaffolds (Brand et al., 2017; Tabdanov et al., 2018). To calculate the elastic 1D modulus, we fitted circular arcs to the peripheral SFs of all analyzed cells and extracted the corresponding arc radii (Figures S2D and S2E). Using the arc radius extracted from the side pattern, the elastic 1D

modulus was found to be EA = 238 nN. We adopted this value for our simulations.

With these parameters, CPM predictions of cell shape during spreading (Figures 1D–1F) aligned nicely with the corresponding experimental measurements (Figures 1A–1C). For the top pattern, we observed qualitatively similar trends between the CPM and the experimentally obtained data (Figures 1C and 1F, open circles); in particular, the spreading of cells that initially adhered to the long edge was much faster than for cells that initially adhered to the short edge. For the side patterns, the differences between the spreading kinetics of cells adhered to either the short or long edge were small both experimentally and computationally (Figures 1C and 1F, filled circles). The simulation captures a delay in spreading at the first corner, but not a slowdown at the second corner (Figure S2A). Overall, the good agreement between experiments and model suggests that the interplay between the gain in cellular adhesion energy and tension is sufficient to explain the global dynamics of cell spreading onto these patterns. In our experimental system, cells always exhibited round arcs during spreading, suggesting that cell shape is determined mainly by the mechanical equilibrium between cortical and peripheral tensions at each time point and that contractility is the main determinant of spreading kinetics for cells with concave shapes bridging adhesive gaps, as assumed in the CPM. This is in contrast to cells spreading on uniformly coated ECM substrates, where actin polymerization and formation of many adhesions over a broad front lead to convex shapes (Burnette et al., 2011; Shemesh et al., 2012).

A Memory of ECM Geometry Is Encoded in the SF Network

We next asked whether the final SF configuration of cells spreading on either pattern depends on the initial adhesive position, thus allowing cells to develop a memory of their spreading history. To answer this question, we tracked SF formation in cells spreading onto the patterns by measuring the mean angular SF orientation relative to the bottom long edge of each pattern. A major issue that complicates this analysis over time is the fact that cells spread on different timelines, creating significant variability in the time of adhesion and initial spreading as well as time spent per corner. To adjust for these offsets, we brought these kinetics into register by identifying specific time points at which cells achieved intermediate spread morphologies that can be used as benchmarks (illustrations in Figures 2A–2D; Figure S5 for spreading rates of individual cells within each specific time point). Specifically, we normalized cells adhering at the long edge of the side pattern by assessing the SF formation starting at time point t_1, where the cell has covered 50% of the pattern and has assumed a triangular shape (Figure 2A, schematic). The mean orientation of SFs in cells attached to the long edge (both top and bottom) of the side patterns was initially approximately 20°. As spreading proceeded, the peak at 20° decreased in frequency (Figure 2A, left graph, light blue to dark blue) and a new peak close to 90° started forming (vertical to the long edges) (Figure 2A, darkest blue curves). Similarly, cells that initially adhered to the short edge of the side patterns were normalized using time point t_1 (Figure 2B, schematic). Cells exhibited an initial mean SF orientation with a peak at approximately 50°, and as the spreading
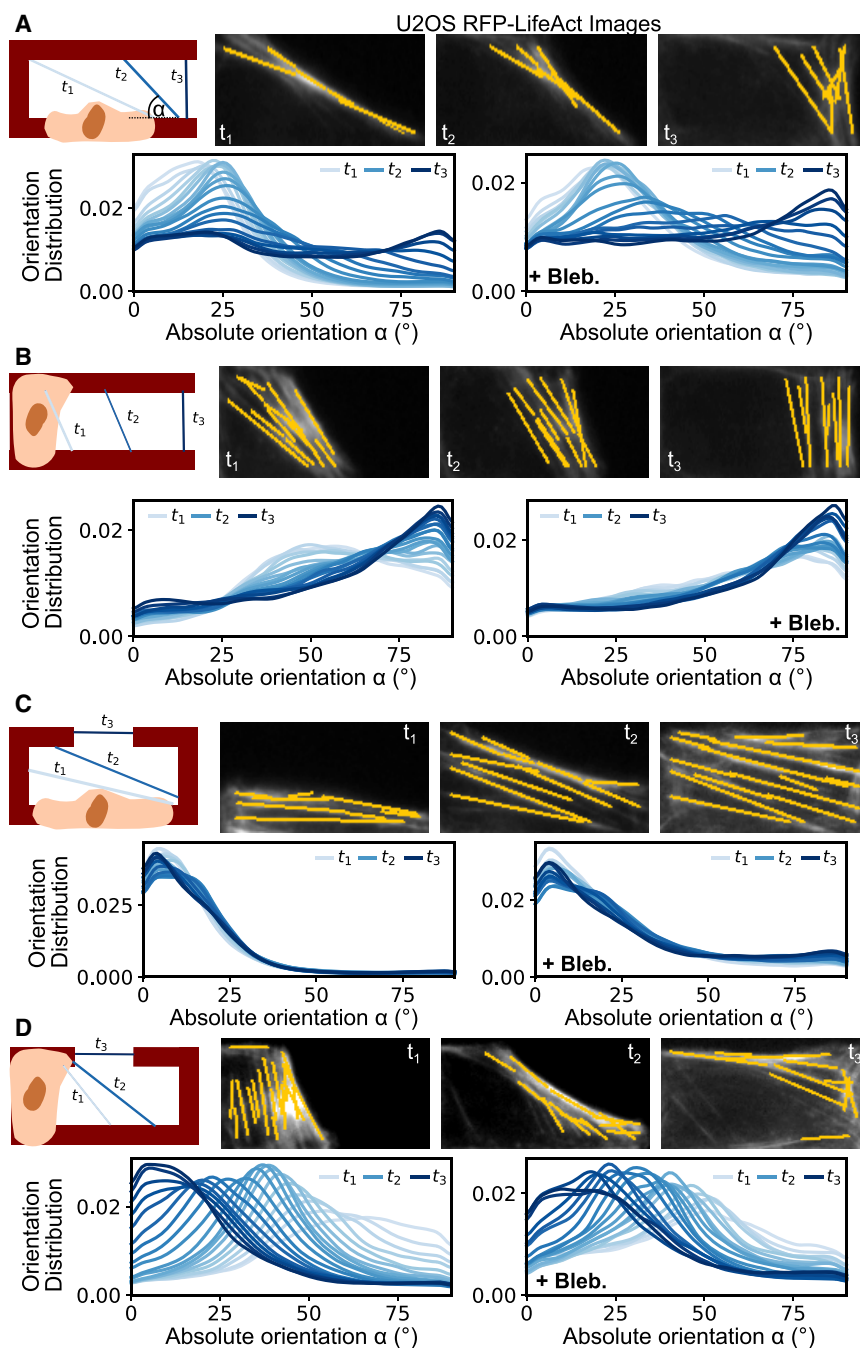
Figure 2. Final SF Orientation Is Dependent on ECM Geometry and Is Independent of the Initial Binding Position

Top row of each panel: schematic showing the time points used to normalize individual cells bound on the short or long edges of each pattern to allow for comparisons to be made. (A) and (B) illustrate adhesion onto a side pattern at the long edge and short edge, respectively. (C) and (D) illustrate adhesion onto a top pattern at the long edge and short edge, respectively. t_1 (light blue) represents the initial time point, t_2 (blue) is an intermediate time point, and t_3 (dark blue) is the final time point at which the cell has spread fully on the pattern. Snapshots show the typical SF architecture, with highlighted SFs at the given time points as given by FilamentSensor. Bottom row of each panel: mean distribution of SF orientations for naive U2OS RFP-LifeAct and blebbistatin-treated U2OS RFP-LifeAct (+ Bleb.) (n = 33, 32, 17, and 56 cells normalized according to schematic for U2OS RFP-LifeAct mean SF orientations; n = 17, 14, 11, and 23 cells normalized according to schematic for blebbistatin-treated U2OS RFP-LifeAct mean SF orientations). Five independent experiments were conducted for the spreading of the U2OS RFP-LifeAct control cells, and 3 independent experiments were conducted for blebbistatin-treated spreading. See also Videos S1 and S2 and Figures S3 and S4.

which was defined by cells fully covering half of the bottom long edge (schematic and representative images in Figure 2D). Cells at t_1 had an initial mean SF orientation with a peak at approximately 40°, and as the spreading process occurred, the mean SF orientation approached 0° (horizontal to the long edge of the pattern) (Figure 2D, left graph). Overall, both binding positions on the top pattern resulted in a mean SF orientation of 0°. We therefore conclude that matrix geometry and initial adhesive position together determine the SF orientation dynamics. This suggests that cells establish a memory of their spreading history through the organization of their SF network.

To quantify how the orientation distributions converge toward the final distribution, we calculated the Kullback-Leibler divergence (see STAR Methods) as a function of time. We compared the angular distribution at each time point to the final configuration and found that the curves start with positive values and approach zero, as expected (Figure S3A). The overall magnitude of the Kullback-Leibler (KL) divergence is much smaller for the side-short and the top-long cases, which is explained by the fact that these cells do not have to turn during the spreading process, again demonstrating that the spreading histories depend strongly on ECM geometry and binding position.

continued, the mean SF orientation approached 90° (vertical to the long edges of the pattern) (Figure 2B, left graph). Thus, both initial adhesive positions on the side pattern evolved toward a final mean SF orientation that approached 90°.

Cells that adhered to the long edge of the top pattern were normalized to time point t_1, where the cell covered 50% of the short edge (Figure 2C, schematic). At t_1, the mean SF orientation was approximately 10°, and as the spreading proceeded, it approached 0° (Figure 2C, left graph). Finally, cells adhering to the short edges of the top patterns were normalized at time point t_1,
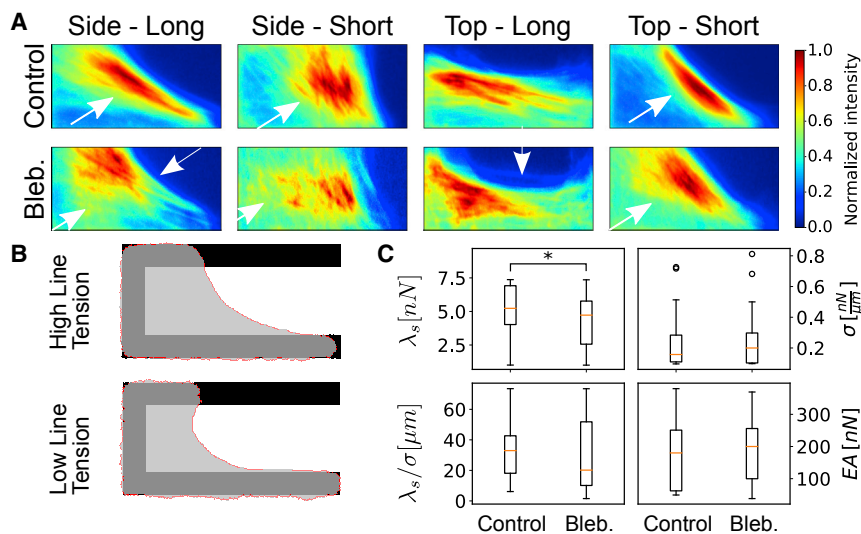
Figure 3. Blebbistatin-Treated Cells Have a Lower Peripheral Line Tension

(A) Average intensities of naive or blebbistatin-treated U2OS cells spreading on each pattern with different initial adhesive positions (intensities of n = 33, 32, 17, and 56 naive cells and n = 17, 14, 11, and 23 blebbistatin-treated cells). White arrowheads point to the arc of the peripheral SF, whereas white arrows point to the confinement of the SF network relative to the peripheral SF (Video S3).

(B) Snapshots from CPM simulations of one cell with higher line tension ($\lambda = 6$ nN, $\sigma = 0.2$ nN/μm, and EA = 300 nN) at the top and lower line tension ($\lambda = 3$ nN, $\sigma = 0.2$ nN/μm, and EA = 100 nN) at the bottom (Video S3).

(C) Comparison of the line tension λ, surface tension σ, and elastic rigidity EA of control and blebbistatin-treated cells. The box represents the 25th and 75th percentiles; whiskers extend from the first datum $>Q1 -1.5*IQR$ to the last datum $<Q3 +1.5*IQR$, with Q1 and Q3 being the first and third quartiles and IQR being the interquartile range. Five independent experiments were conducted for the spreading of the U2OS RFP-LifeAct control cells, and 3 independent experiments were conducted for blebbistatin-treated spreading.

See also Figure S2 and Table S1 for statistical comparisons.

Cells with Mild Blebbistatin Treatment Show Faster Spreading Kinetics and a Less-Well-Defined Actin Cytoskeleton

Based on the CPM simulations (Figure 1), we conclude that contractility is the main determinant of spreading over non-adhesive regions. For homogeneously coated ECM substrates, some studies have shown that reduced contractility increases the extent and/or rate of spreading (Cai et al., 2010), while others showed no effect (Dillard et al., 2014). We therefore repeated our experiments in the presence of 3 μM blebbistatin, an NMMII inhibitor (Figure S2A; Video S3). Application of blebbistatin in the usual dose range of 10–50 μM completely inhibited cell spreading and/or SF assembly (data not shown), requiring us to apply a much smaller dose (Bischofs et al., 2008; Aratyn-Schaus and Gardel, 2010; Pasapera et al., 2010; Aratyn-Schaus et al., 2011). Such low-dose blebbistatin treatments have previously been used to investigate actin flow on patterned cells (Kumar et al., 2014). Blebbistatin-treated cells spreading on the side patterns exhibited fewer SFs and increased peripheral SF curvature (Video S3, C and D) as compared to control cells (Video S1, C and D). The same observations were true for blebbistatin-treated cells spreading on the top patterns (Video S3, A and B) as compared to control cells (Video S1, A and B). We also observed that the relations between spreading rates and initial adhesive positions on each pattern remained the same. Specifically, cells that initially adhered to the long edge of the top pattern spread faster than cells that adhered to the short edges (Figure S2C, blue bars), whereas cells spread with similar kinetics on the side pattern, irrespective of binding position (Figure S2C, blue bars). Finally, we observed similar spreading kinetics between blebbistatin-treated U2OS and control cells (Figures S2B and S2C).

Given the qualitative differences observed in SF architecture, we wondered whether blebbistatin-treated cells also established

a memory of spreading history via SF network organization. Compared to the mean SF orientation of control cells, the mean SF distributions of blebbistatin-treated cells underwent similar transitions for all starting positions and patterns during cell spreading, evolving toward a preferred SF orientation perpendicular to the direction of the missing edge of the pattern (Figure 2, "+ Bleb." graphs). Specifically, cells spreading on top patterns transitioned closer to 0°, whereas cells on side patterns transitioned closer to 90° orientations. The peaks of the final SF distributions (dark blue), however, were not as sharp as those observed in control cells, especially for cells spreading on top patterns. The width of the dark blue curve suggests that after spreading, cells reorient their SFs to transition the mean SF orientation toward 90°—in other words, vertical SFs—for all patterns. Moreover, when comparing the divergence of U2OS versus blebbistatin-treated U2OS cells at each time point (Figure S3B), the angular distributions do not approach one another significantly over time. This suggests that while control and blebbistatin-treated cells spread with similar mean SF orientations, blebbistatin-treated cells do so faster and develop less-well-defined SF networks.

Blebbistatin Treatment Lowers the Line Tension of Peripheral SFs

To qualitatively visualize the average effect of blebbistatin compared to control cells, we overlaid the SF network architecture of all of the analyzed cells at time point t_2 (as shown in Figure 2). The average SF intensity of blebbistatin-treated cells spreading on the side pattern (Figure 3A) exhibited a more invaginated arc than control cells (Figure 3A, white arrowhead), in agreement with earlier results (Bischofs et al., 2008). Moreover, the SF network was not confined to the spreading edge as tightly as in control cells (white arrows). Similarly, the average SF
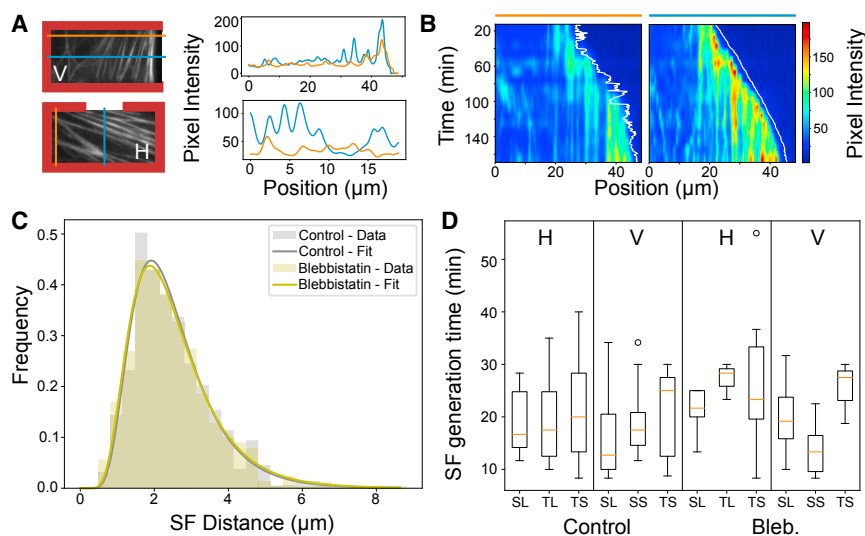
Figure 4. Both Control and Blebbistatin-Treated Cells Form SFs at Spatial Intervals of ~2.5 μm and Temporal Intervals of ~15 min

(A) LifeAct intensities of spreading cells registered along horizontal and vertical lines close to the FN lines of the pattern, depicted in orange (close to boundary) and blue (center of the pattern). We separately categorized distances between horizontal SFs ("H" distances) and distances between vertical SFs ("V" distances). The plots on the right are intensity profiles across the color-coded lines for the 2 example images.

(B) Representative spatiotemporal plots of the image intensities along a horizontal line showing the occurrence of SFs of an individual control cell bound on the short edge of the side pattern, for the line close to the boundary (orange line) and the line in the center (blue line).

(C) The spatial distances between SFs follow a log-normal distribution with mean μ = 2.5 ± 1.0 μm for naive U2OS cells and μ = 2.5 ± 1.1 μm for blebbistatin-treated cells.

(D) The average temporal distance between subsequent SFs is T = 1.58 ± 11.1 min and T = 14.2 ± 12.5 min for control and blebbistatin-treated cells, respectively (first letter: S, side pattern; T, top pattern; second letter: L, long edge binding; S, short edge binding). Mann-Whitney non-parametric tests were performed to determine statistical differences between conditions and no statistical differences were observed. n = 16, 15, 9, and 25 naive cells and n = 15, 9, 3, and 16 blebbistatin-treated cells in the order side-long (SL), side-short (SS), top-long (TL), and top-short (TS) were analyzed. The box represents the 25th and 75th percentiles; whiskers extend from the first datum >Q1 −1.5*IQR to the last datum <Q3 +1.5*IQR, with Q1 and Q3 being the first and third quartiles and IQR being the interquartile range. Five independent experiments were conducted for the spreading of the U2OS RFP-LifeAct control cells, and 3 independent experiments were conducted for blebbistatin-treated spreading.

See also Figure S4.

intensity of blebbistatin-treated cells spreading on the top pattern also exhibited increased curvature (white arrows in Figure 3A). Specifically, we observed a rearrangement of SFs to favor shorter (perpendicular to the spacing) SFs for cells bound on the long edge of the top pattern (Figure 3A).

We next used the CPM to arrive at a quantitative characterization of the effects of blebbistatin treatment. To this end, we used a minimization procedure (see STAR Methods) to determine a set of parameter values for each experimentally obtained trajectory. By calculating the deviation between the spatiotemporal evolution of the cellular envelope of experimentally recorded cells and a series of simulated cells, we were able to determine stresses and elastic moduli for each cell and compare control versus blebbistatin-treated cells. Overall, we found that our mild blebbistatin treatment resulted in a significantly lower line tension, but it did not influence the surface tension or the rigidity of the free arcs (Figures 3B and 3C; see Table S1 for statistical analysis performed using the Mann-Whitney test). To visualize the effects of lower line tension, we ran simulations with varying line tension parameters (Figure 3B; Video S4). By shifting to low values, we observed that the simulated free arc showed more pronounced curvature, which was also observed in individual blebbistatin-treated U2OS cells during spreading (Video S3). Furthermore, the contour appeared more uneven, which is due to stochastic effects in the model. Overall, our analysis confirms that the low dose of blebbistatin used in these experiments leads to cells that exhibit a lower line tension (NMMII contractility in peripheral SFs), with little to no significant effects on the surface tension (NMMII contractility in the cortex).

SFs Are Generated with Typical Separations in Space and Time that Are Independent of ECM Geometry and Initial Adhesive Position

To characterize the SF network formation more quantitatively, we took advantage of the fact that the observed spreading dynamics are composed of stretches of 1D processes, namely spreading along 1 leg of the pattern. We first drew a line parallel to the FN lines of each pattern and recorded the changes in pixel intensity over time as the cell was spreading (Figure 4A, orange and blue lines). The distances between horizontal SFs were labeled as "H" distances, whereas distances between vertical SFs were labeled as "V" distances. By computing the distance between the observed intensity peaks (Figure 4A, right panel), we determined the distance between subsequent SFs (which also corresponds to the distance between mature FAs along the FN line), as well as the distance at which the cell creates a new SF. We also displayed the information as a time sequence of intensity profiles (Figure 4B, left panel). On average, cells generated 6 horizontal and 12 vertical SFs during the spreading process, irrespective of the pattern geometry or starting position (Figure S4). These numbers suggest that the average distance between subsequent SFs does not depend on SF length. Moreover, blebbistatin treatment did not significantly influence these numbers. Comparing the distribution of distances between subsequent SFs for all of the binding positions on both top and side patterns, we observed that the experimental data were well described by a log-normal distribution with mean μ = 2.5 ± 1.0 μm for control and μ = 2.5 ± 1.1 μm for blebbistatin-treated cells (Figure 4C). Finally, we observed that the average time
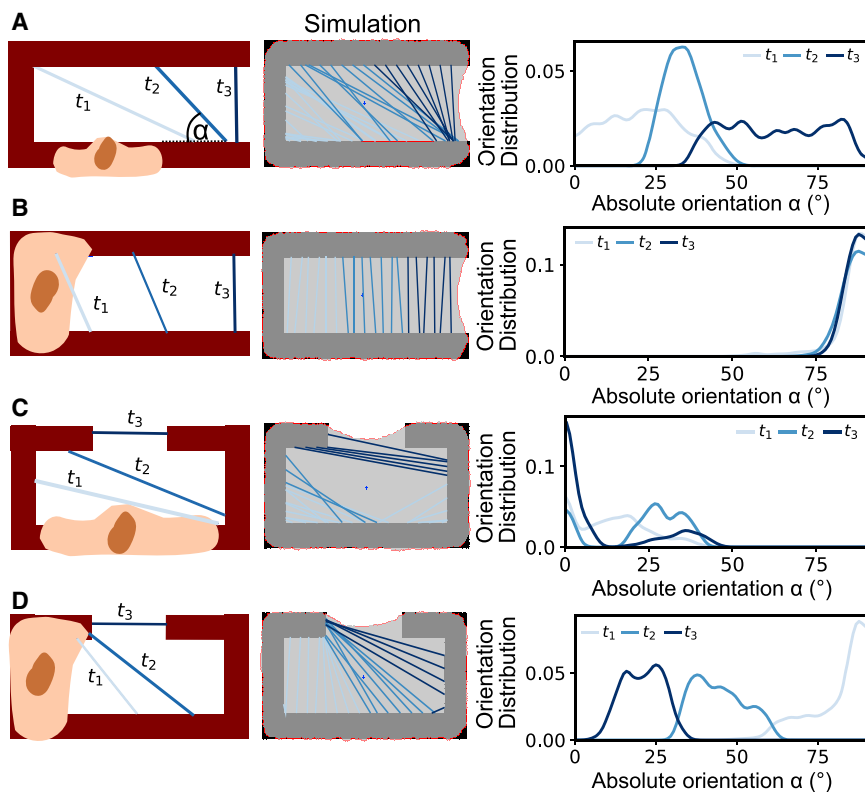
Figure 5. Simulation of SF Distribution during Cell Spreading on Each Pattern
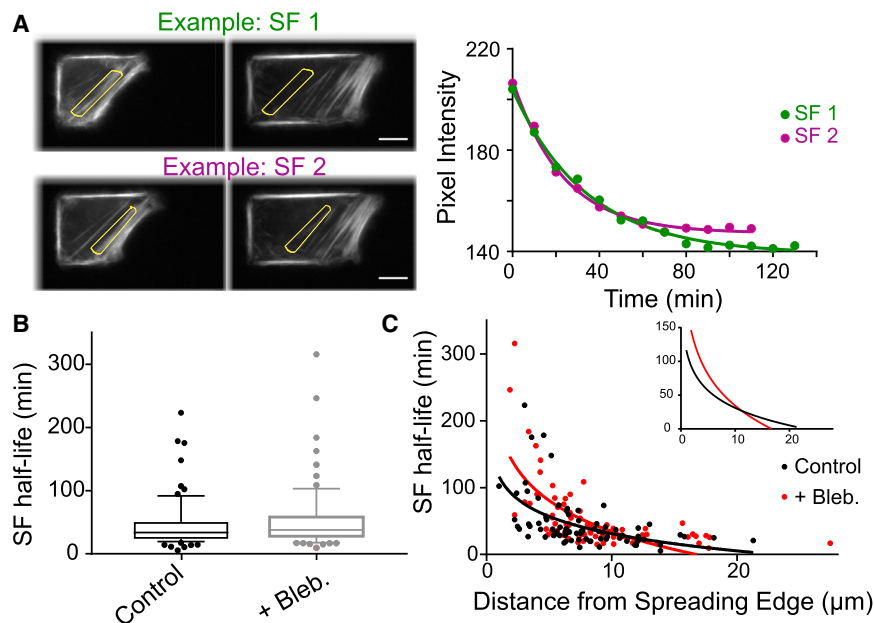
The first and second rows illustrate adhesion onto a side pattern at the long edge (A) and short edge (B). The third and fourth rows illustrate adhesion onto a top pattern at the long edge (C) and short edge (D). Left column: schematic showing the time points used to normalize individual cells adhered to the short or long edge of each pattern to allow for comparisons to be made. t_1 (light blue) represents the initial time point, t_2 (blue) is an intermediate time point, and t_3 (dark blue) is the final time point at which the cell has spread fully on the pattern. Center column: simulated SF architecture using a modified CPM with color-coded SFs, using light blue for time point t_1 and dark blue for time point t_3. Right column: simulated mean distribution of SF orientations. See also Figure S5.

elapsed between the assembly of subsequent SFs is T = 15.8 ± 11.1 min and T = 14.2 ± 12.5 min for control and blebbistatin-treated cells, respectively (Figure 4D). Based on these results, we conclude that cells generate SFs perpendicular to the direction of spreading at an average spatial separation distance of ~2.5 μm and a temporal interval of ~15 min, and that small concentrations of blebbistatin do not strongly alter these spatial and temporal scales.

SF Architecture during Cell Spreading Is Predicted by the CPM with a Simple Rule for the Formation of Internal SFs

As described above, our CPM is sufficient to predict cell shape dynamics during spreading (Figure 1), indicating that these trajectories can be fully explained by the balance between adhesive energy and the different types of cell tension. Moreover, we have shown that new SFs are locally generated by a stereotypical process that is independent of the details of the spreading trajectory (Figure 4). We therefore hypothesized that the CPM augmented by simple rules for periodic SF formation should be sufficient to predict the SF orientation distribution measured experimentally (Figure 2). Internal SFs were introduced into the CPM as straight lines between 2 FAs that anchor an arc above the non-adhesive areas and were defined to appear as soon as they laid completely within the cell body. This encapsulates the idea that internal SFs are formed as transverse arcs behind the advancing front and later straighten due to NMMII contractility and surface anchorage. We incorporated a minimum distance between SFs at the faster-spreading side of the cell, as sug-

gested by our quantitative image analysis (Figure 4). Note that according to these simple rules, internal SFs have no influence on the spreading process, although the underlying feedback processes are contained in the experimental observation of a typical distance between subsequent SFs (see STAR Methods for more details). With this simple ansatz, we are able to predict the experimentally observed distributions (Figure 5). We found that cells that initially adhered to the long edges of the side pattern had an initial SF configuration that peaked at ~20° (light blue SFs), and as the spreading continued, the SF configuration (darker shades of blue) switched to 90° (vertical to the long edges and parallel to the spacing) (Figure 5A). However, cells adhering to the short edge of the side pattern exhibited vertical SF configurations throughout the spreading process (Figure 5B). For the top pattern, cells adhering to the long edge exhibited an initial SF configuration peaking at ~15° (light blue), and as the spreading process continued, the configuration of most SFs converged to 0° (horizontal to the long edge) (Figure 5C, darker shades of blue). It should be noted that in the simulation, a second peak appears at ~30°, which is not observed experimentally. We hypothesize that this is because most simulated cells undergo a symmetry break during spreading and reach one free corner of the pattern before the other. Intermediate SFs with a diagonal orientation are therefore incorporated between the newly occupied corner and a point along the long edge. Finally, cells initially adhered to the short edge of the top pattern showed a vertical initial SF configuration, and with increasing time, the SF configuration first approached a diagonal and then a horizontal configuration (0°) (Figure 5D). The superposition of SF distributions onto our earlier CPM simulations of spreading cells (Figure S5) illustrates that SFs track the advancing front and store a memory of the turning process affected by the combination of pattern geometry and initial position. Overall, we conclude that a simple CPM for cell shape dynamics augmented with a simple rule for geometrically defined formation of SFs based on experimental

Figure 6. SFs Farther Away from the Spreading Edge Decay More Rapidly

(A) Representative examples of SF half-life time constant measurements. An SF is selected by drawing a region of interest (ROI) around it; the fluorescence pixel intensity over time is plotted and fitted to an exponential decay to obtain an SF half-life time constant. Scale bar, 10 μm.

(B) SF half-life time constant measurements from control and blebbistatin-treated U2OS cells. The box represents the 25th and 75th percentiles; the whiskers represent the 10th and 90th percentiles. No statistical difference was observed between the 2 conditions (Mann-Whitney; p = 0.24).

(C) SF half-lives plotted against the distance of the SF from the spreading edge at the time of the first fluorescent pixel intensity measurement. SFs from cells adhered to both the top and the side pattern were used for the measurements. Control cells depicted as black circles; top pattern: 39 SFs from 18 cells; side pattern: 44 SFs from 23 cells. Bleb-bistatin-treated cells depicted as red circles; top pattern: 46 SFs from 20 cells; side pattern: 33 SFs from 12 cells. A negative correlation was observed between SF half-life and the distance to the spreading edge (control: Spearman correlation for both patterns, both binding positions: ρ = −0.60, p < 0.0001; blebbistatin-treated cells: Spearman correlation for both patterns, both binding positions: ρ = −0.71, p < 0.0001). The data were fit to a semi-log equation; for clarity, the fitted lines are depicted in the inset without the data points (control: y = −85.56log(x) + 116.7; blebbistatin-treated: y = −153.7log(x) + 188.1). Five independent experiments were conducted for the spreading of the U2OS RFP-LifeAct control cells, and 3 independent experiments were conducted for blebbistatin-treated spreading.

See also Figure S6.

observations can robustly predict SF orientations observed during cell spreading.

SF Half-Life Depends on the Distance from the Spreading Edge and Is Regulated by NMMII Contractility

Because the cytoskeleton is continuously turning over, we asked how long the memory of spreading history persists within the SF network. By measuring the pixel intensity of already formed SFs over time, we defined an SF half-life measurement as the time constant over which 63.2% of the fluorescence intensity disappears (Figure 6A). We performed these measurements for control and blebbistatin-treated cells spreading on top and side patterns (irrespective of initial position) and found a typical timescale of 50 min. More specifically, we observed a slight increase in the SF half-lifetime constants of blebbistatin-treated cells (mean ± SE of control: 45.6 ± 4.33 min and of blebbistatin-treated cells: 53.3 ± 5.61 min; Mann-Whitney non-parametric test, p = 0.24) (Figure 6B). While this increase was not significant, we hypothesized that differences may be masked by the large variation in the data, which may in turn be due to a systematic dependence of the SF half-life on its spatial position in the cell. To explore this possibility, we plotted the half-life of SFs in cells spreading on top and side patterns relative to the distance of the observed SF from the spreading edge at the time point of the first pixel intensity measurement (Figure 6C). Overall, we observed a negative non-linear correlation for control and blebbistatin-treated cells, suggesting that SFs farther away from the spreading edge disintegrate faster, irrespective of pattern geometry. The semi-log fit

of the blebbistatin-treated cells (inset in Figure 6C) was shifted to the right for all pattern types and initial adhesive positions. SFs closer to the edge exhibited higher SF half-life time constants in blebbistatin-treated cells compared to SFs in control cells (Figure S6). Overall, our data suggest that cells encode a memory of their spreading history within their SF network that lasts for ~50 min. This memory is regulated by myosin contractility that breaks down SFs that are far away from the leading edge, because the inhibition of myosin produces SFs that persist more deeply into the cell interior.

Cell Spreading on a Network of Collagen Fibers Also Shows Localized Lamellipodia and Invaginated Arc Morphology

To determine whether the observations seen on our micropatterns are predictive of spreading behavior on matrices featuring fibers, which are a common feature of 3D scaffolds, we examined cell spreading along 2D networks of collagen fibers. We formed these fiber arrays by tethering collagen I to polyacrylamide gels using 2-pyridinecarboxaldehyde-based ligation (2PCA-AA gels), which we previously showed supports fiber assembly beyond the levels that are seen with standard side chain amine-based conjugation (Lee et al., 2016). After seeding, cells exhibited the same initial round shape as on the patterns (Figures S7A and S7B). Over time, cells spread and formed invaginated arcs by interacting with the collagen fibers (Figures 7A [cells fixed after spreading], 7B, and S7 [timelapse of cell spreading]). Similar to spreading on micropatterns, we did not observe the broad lamellipodia normally seen on homogeneously coated
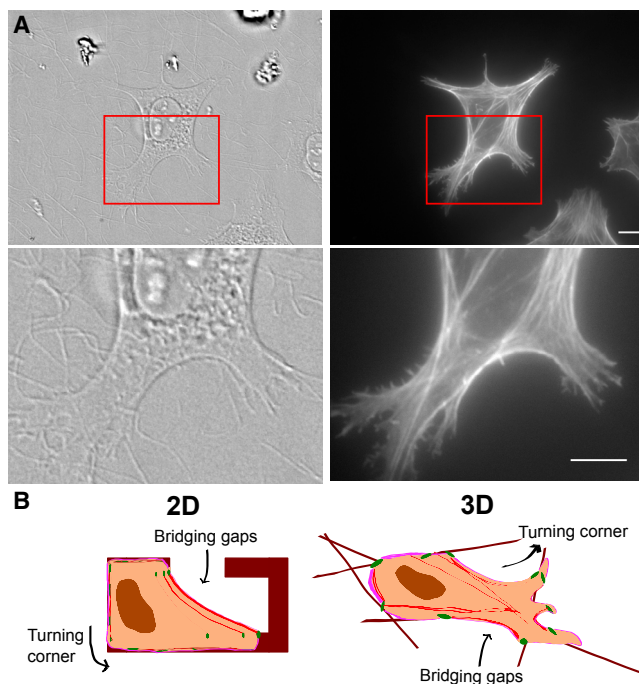
Figure 7. U2OS Cell Spreading on Collagen-Coated 2PCA-AA Gels Resembles Spreading on Micropatterned Legs

(A) Differential interference contrast (left column) and epifluorescence Lifeact (right column) imaging of protrusions, collagen fibers, and SFs in cells fixed after being allowed to spread. Top row: U2OS RFP-Lifeact cell interacting with collagen fibers. Protrusions form along collagen fibers. Interior SFs are often observed to align with collagen fibers. Bottom row: higher-magnification view of the boxed region. One biological replicate was conducted at this 2PCA-AA gel stiffness. Scale bar, 10 μm. See also Figure S7.

(B) Illustration depicting the commonalities of cell spreading on 2D patterns and 3D fibers. In both cases, the cell encounters corners that require rotation and bridging of gaps that are connected by peripheral SFs.

substrates and instead observed multiple lamellipodia along collagen fibers, analogous to spreading across the legs of the micropatterns (Figures 7A, 7B, and S7). There were also notable differences between spreading on 2PCA-AA gels and the micropatterns. Whereas the micropatterns gave rise to families of parallel SF bundles behind the peripheral arc, these structures were less regular and less frequent on the collagen fiber arrays (Figures 7A and 7B). This may be due to the collagen fibers being flexible enough to be deformed by actomyosin contraction. Another essential difference between the 2 paradigms is that the micropatterns only permit the formation of 2 lamellipodia, whereas collagen surfaces permit the formation of multiple lamellipodia, creating additional cell-to-cell heterogeneity in spreading. Nonetheless, the dynamics of spreading on collagen fibers are more similar to results from micropatterns than from homogeneous 2D matrices, supporting the biological relevance of our observations on micropatterns.

DISCUSSION

We have explored how ECM geometrical cues influence the kinetics of cellular spreading and the spatiotemporal evolution of

the SF network. Previous work on cellular spreading has concentrated on homogeneously coated substrates such as nanoporous hydrogels or tissue culture plastic (Engler et al., 2004; Giannone et al., 2004; Reinhart-King et al., 2005; Nisenholz et al., 2014; Diz-Muñoz et al., 2016; Pontes et al., 2017). Cells *in vivo*, however, tend to adhere, spread, and migrate along geometrically defined ECM structures. Thus, understanding how cells sense and respond to such matrix cues can provide important insights into cellular processes associated with development, wound healing, and cancer metastasis. However, such mechanistic insights are prohibitively difficult to obtain from true 3D matrices, given the challenges associated with high-resolution quantitative imaging in such matrices. Our adhesive micropatterns combine the defining features of migration in 3D matrices, such as corner turning and matrix bridging, with the high-resolution experimental accessibility of 2D matrices. By combining these patterns and SF time-lapse imaging, we were able to control cell spreading onto structured matrices and to quantitatively validate and mechanistically dissect our observations through mathematical modeling.

We first found that cell spreading depends on ECM geometry and the initial adhesive position. For example, the presence of corners in the ECM slows cell spreading due to cell rotation. Although this coordination between spreading trajectory and matrix architecture would not be observed in cells spreading on isotropic matrices, it is very common for cell spreading in fibrous 3D environments such as collagen gels (Owen et al., 2017). On the subcellular level, we showed that the evolving SF network architecture is tightly controlled by ECM geometry and initial cell position. Specifically, SFs are locally aligned predominantly in parallel to the orientation of the advancing edge, revealing that cells can encode the memory of their spreading history within their SF architecture.

Given that cell spreading on structured matrices seems to follow clear rules, we set out to predict spreading with a simple CPM for shape dynamics dominated by NMMII contractility. To also predict the SF orientation distribution, we complemented this CPM with a simple geometrical rule based on the experimental observation that new SFs are formed with a constant characteristic distance. The success of the CPM in predicting spreading trajectory and SF network orientation distribution demonstrates that the interplay between gain in adhesion energy and cell tension is sufficient to explain the mechanistic aspects of spreading such as SF assembly behind the leading edge. In contrast to cell spreading on homogeneous substrates, we do not need a model for lamellipodial protrusion, which on the patterns is restricted to the two endpoints of the advancing arc. Based on the CPM, we were also able to extract the line tension, surface tension, and rigidity of the cellular arc during cell spreading. In particular, we showed that low concentrations of blebbistatin, which allow for cell spreading and SF formation, decreased the line tension of cell spreading edges, but did not alter the edge bundle rigidity and the surface tension in a detectable manner. This is in agreement with earlier results that showed that peripheral SFs are more susceptible to blebbistatin treatment than the cell cortex (Bischofs et al., 2008; Labouesse et al., 2015; Tabdanov et al., 2018). In the future, our findings may be further expanded by creating a model for predicting

spreading in 3D fiber environments, in which we take into full consideration the typical spacing and angles between individual fibers in the fibrous environment.

The formation of FAs and SFs on homogeneous substrates has previously been found to proceed in a stereotypical and oscillatory manner (Giannone et al., 2004; Burnette et al., 2011). We observed similar periodic processes in our structured substrates. During spreading on our patterns, SFs formed periodically at spatial intervals of ∼2.5 μm and temporal intervals of ∼15 min. Moreover, SFs farther away from the spreading edge disassembled at a faster rate than those closer to the edge, and this negative feedback loop is partially regulated by myosin contractility. It is important to note that the spatiotemporal kinetics of SF generation are conserved across both patterns and all initial adhesive positions. This is surprising because although it has been argued that the actin cytoskeleton behaves like a locally excitable medium (Bement et al., 2015; Graessl et al., 2017), one also expects global features to play a regulatory role (e.g., through membrane tension) (Diz-Muñoz et al., 2016). One aspect of this unexpected result may be that in our case, the lamellipodium is restricted to a small region during spreading along the legs. While we recognize that membrane tension is an important regulator of cell spreading, it remains very challenging to measure this parameter in a spatially resolved fashion (Lieber et al., 2013, 2015), which is necessary as it has recently been argued that local changes in membrane tension do not propagate globally due to coupling to the cortex (Shi et al., 2018). In the future, it may be fruitful to incorporate newly developed optical tension sensors (Colom et al., 2018).

We also found that cells can retain a memory of their spreading history through the SF network on a timescale of 50 min. While earlier work has hinted at the idea that cells exploit adhesive position to "remember" earlier shapes (Théry et al., 2007), the concept that memory can be encoded in the actin cytoskeleton is novel relative to current paradigms that focus on the importance of biochemical or genetic networks. The 50-min timescale measured here is reminiscent of the 50-min timescale recently identified in an optogenetic study of SF elasticity (Oakes et al., 2017). An open yet very important question is which SF architecture prevails once memory is lost. In our system, the answer to this question is obscured to some degree by cell division, which often starts once complete spreading has been achieved. Internal SFs retained their orientation (top pattern = parallel to long FN edge, side pattern = perpendicular to long FN edge) until the onset of division, at which point internal SFs disintegrated (Video S5). Given that matrix and actin geometry have been shown to regulate mitotic spindle positioning and the axis of division (Théry et al., 2005), it would be interesting to investigate whether a spreading history-dependent mechanism influences the orientation of daughter cells.

Finally, we showed that cell spreading on networks of collagen fibers showed many similarities with cell spreading on our micropattern assay, including spatially localized lamellipodia and spreading with an invaginated arc at the front. However, a distinct difference across these 2 paradigms is the lack of periodicity in the formation of new SFs. We hypothesize that this discrepancy may arise from the deformability of the collagen fibers and the allowance of >2 lamellipodia due to the reduced geometrical control.

Future studies are needed to test these hypotheses. Recently introduced printing techniques to engineer networks of FN (Wang et al., 2018) or collagen lines (Tabdanov et al., 2018) may be valuable in this regard, but these assays do not allow for *in situ* self-assembly or remodeling of ECM proteins as our collagen assay does. Fiber electrospinning (Chen et al., 2019) or direct laser writing (Brand et al., 2017) may provide an ideal approach through its combination of pattern control and fiber deformability.

In summary, our work quantitatively characterizes spreading kinetics on heterogeneously structured ECM substrates through the use of adhesive micropatterns and quantitative image analysis. The distribution of SF orientations can be closely predicted by a CPM augmented by a simple geometrical rule for forming new SFs. Our findings suggest that similar stereotypical processes are also at play in 3D environments, particularly in cases in which cells must spread along discrete fibers or fiber bundles. They also suggest that corners may be a limiting bottleneck in spreading in 3D fibrous environments, which *in vivo* may be overcome by elasticity. However, our model also suggests that elastic line tensions in the cell contour may help to bridge non-adhesive regions, and this effect should be enhanced in stiffer environments. It remains an open question as to how fiber deformability may modulate the results presented here. A valuable starting point for exploring these issues may be represented by 1D nanofibers or 3D elastic scaffolds (Klein et al., 2010; Estabridis et al., 2018).

STAR★METHODS

Detailed methods are provided in the online version of this paper and include the following:

- KEY RESOURCES TABLE
- CONTACT FOR REAGENT AND RESOURCE SHARING
- EXPERIMENTAL MODEL AND SUBJECT DETAILS
- METHOD DETAILS
  - Deep-UV based micropattern fabrication
  - Fluorescence time lapse experiments of cell spreading
  - DIC Time Lapse experiments of cell spreading (Figure S1)
  - U2OS cells spreading on 2PCA-polyacrylamide gels conjugated with collagen (Figures 7 and S7)
  - Quantification of cell area analysis (Figures 1 and S2)
  - SF angle analysis (Figures 2, S3, and S4)
  - Segmentation of SFs
  - SF distance analysis (Figures 4 and S4)
  - SF lifetime analysis (Figures 6 and S6)
  - Model Description (Figures 1, 3, and 5)
  - Fit of model parameters to experiments
- QUANTIFICATION AND STATISTICAL ANALYSIS

SUPPLEMENTAL INFORMATION

Supplemental Information can be found online at https://doi.org/10.1016/j.celrep.2019.04.035.

REFERENCES

Albert, P.J., and Schwarz, U.S. (2014). Dynamics of cell shape and forces on micropatterned substrates predicted by a cellular Potts model. Biophys. J. *106*, 2340–2352.

Albert, P.J., and Schwarz, U.S. (2016a). Dynamics of Cell Ensembles on Adhesive Micropatterns: Bridging the Gap between Single Cell Spreading and Collective Cell Migration. PLoS Comput. Biol. *12*, e1004863.

Albert, P.J., and Schwarz, U.S. (2016b). Modeling cell shape and dynamics on micropatterns. Cell Adhes. Migr. *10*, 516–528.

Aratyn-Schaus, Y., and Gardel, M.L. (2010). Transient frictional slip between integrin and the ECM in focal adhesions under myosin II tension. Curr. Biol. *20*, 1145–1153.

Aratyn-Schaus, Y., Oakes, P.W., and Gardel, M.L. (2011). Dynamic and structural signatures of lamellar actomyosin force generation. Mol. Biol. Cell *22*, 1330–1339.

Azioune, A., Carpi, N., Tseng, Q., Théry, M., and Piel, M. (2010). Protein micropatterns: a direct printing protocol using deep UVs. Methods Cell Biol. *97*, 133–146.

Barnhart, E.L., Allard, J., Lou, S.S., Theriot, J.A., and Mogilner, A. (2017). Adhesion-Dependent Wave Generation in Crawling Cells. Curr. Biol. *27*, 27–38.

Bement, W.M., Leda, M., Moe, A.M., Kita, A.M., Larson, M.E., Golding, A.E., Pfeuti, C., Su, K.C., Miller, A.L., Goryachev, A.B., and von Dassow, G. (2015). Activator-inhibitor coupling between Rho signalling and actin assembly makes the cell cortex an excitable medium. Nat. Cell Biol. *17*, 1471–1483.

Bischofs, I.B., Klein, F., Lehnert, D., Bastmeyer, M., and Schwarz, U.S. (2008). Filamentous network mechanics and active contractility determine cell and tissue shape. Biophys. J. *95*, 3488–3496.

Bischofs, I.B., Schmidt, S.S., and Schwarz, U.S. (2009). Effect of adhesion geometry and rigidity on cellular force distributions. Phys. Rev. Lett. *103*, 048101.

Blanchoin, L., Boujemaa-Paterski, R., Sykes, C., and Plastino, J. (2014). Actin dynamics, architecture, and mechanics in cell motility. Physiol. Rev. *94*, 235–263.

Brand, C.A., Linke, M., Weißenbruch, K., Richter, B., Bastmeyer, M., and Schwarz, U.S. (2017). Tension and Elasticity Contribute to Fibroblast Cell Shape in Three Dimensions. Biophys. J. *113*, 770–774.

Burnette, D.T., Manley, S., Sengupta, P., Sougrat, R., Davidson, M.W., Kachar, B., and Lippincott-Schwartz, J. (2011). A role for actin arcs in the leading-edge advance of migrating cells. Nat. Cell Biol. *13*, 371–381.

Cai, Y., Rossier, O., Gauthier, N.C., Biais, N., Fardin, M.A., Zhang, X., Miller, L.W., Ladoux, B., Cornish, V.W., and Sheetz, M.P. (2010). Cytoskeletal coherence requires myosin-IIA contractility. J. Cell Sci. *123*, 413–423.

Carey, S.P., Starchenko, A., McGregor, A.L., and Reinhart-King, C.A. (2013). Leading malignant cells initiate collective epithelial cell invasion in a three-dimensional heterotypic tumor spheroid model. Clin. Exp. Metastasis *30*, 615–630.

Chen, T., Callan-Jones, A., Fedorov, E., Ravasio, A., Brugués, A., Ong, H.T., Toyama, Y., Low, B.C., Trepat, X., Shemesh, T., et al. (2019). Large-scale curvature sensing by directional actin flow drives cellular migration mode switching. Nat. Phys. *15*, 393–402.

Colom, A., Derivery, E., Soleimanpour, S., Tomba, C., Molin, M.D., Sakai, N., González-Gaitán, M., Matile, S., and Roux, A. (2018). A fluorescent membrane tension probe. Nat. Chem. *10*, 1118–1125.

Cukierman, E., Pankov, R., Stevens, D.R., and Yamada, K.M. (2001). Taking cell-matrix adhesions to the third dimension. Science *294*, 1708–1712.

Dillard, P., Varma, R., Sengupta, K., and Limozin, L. (2014). Ligand-mediated friction determines morphodynamics of spreading T cells. Biophys. J. *107*, 2629–2638.

Diz-Muñoz, A., Thurley, K., Chintamen, S., Altschuler, S.J., Wu, L.F., Fletcher, D.A., and Weiner, O.D. (2016). Membrane Tension Acts Through PLD2 and mTORC2 to Limit Actin Network Assembly During Neutrophil Migration. PLoS Biol. *14*, e1002474.

Doyle, A.D., and Yamada, K.M. (2016). Mechanosensing via cell-matrix adhesions in 3D microenvironments. Exp. Cell Res. *343*, 60–66.

Doyle, A.D., Wang, F.W., Matsumoto, K., and Yamada, K.M. (2009). One-dimensional topography underlies three-dimensional fibrillar cell migration. J. Cell Biol. *184*, 481–490.

Doyle, A.D., Carvajal, N., Jin, A., Matsumoto, K., and Yamada, K.M. (2015). Local 3D matrix microenvironment regulates cell migration through spatiotemporal dynamics of contractility-dependent adhesions. Nat. Commun. *6*, 8720.

Eltzner, B., Wollnik, C., Gottschlich, C., Huckemann, S., and Rehfeldt, F. (2015). The filament sensor for near real-time detection of cytoskeletal fiber structures. PLoS One *10*, e0126346.

Engler, A., Bacakova, L., Newman, C., Hategan, A., Griffin, M., and Discher, D. (2004). Substrate compliance versus ligand density in cell on gel responses. Biophys. J. *86*, 617–628.

Estabridis, H.M., Jana, A., Nain, A., and Odde, D.J. (2018). Cell Migration in 1D and 2D Nanofiber Microenvironments. Ann. Biomed. Eng. *46*, 392–403.

Gardel, M.L., Schneider, I.C., Aratyn-Schaus, Y., and Waterman, C.M. (2010). Mechanical integration of actin and adhesion dynamics in cell migration. Annu. Rev. Cell Dev. Biol. *26*, 315–333.

Giannone, G., Dubin-Thaler, B.J., Döbereiner, H.G., Kieffer, N., Bresnick, A.R., and Sheetz, M.P. (2004). Periodic lamellipodial contractions correlate with rearward actin waves. Cell *116*, 431–443.

Graessl, M., Koch, J., Calderon, A., Kamps, D., Banerjee, S., Mazel, T., Schulze, N., Jungkurth, J.K., Patwardhan, R., Solouk, D., et al. (2017). An excitable Rho GTPase signaling network generates dynamic subcellular contraction patterns. J. Cell Biol. *216*, 4271–4285.

Grinnell, F., and Petroll, W.M. (2010). Cell motility and mechanics in three-dimensional collagen matrices. Annu. Rev. Cell Dev. Biol. *26*, 335–361.

Gupton, S.L., and Waterman-Storer, C.M. (2006). Spatiotemporal feedback between actomyosin and focal-adhesion systems optimizes rapid cell migration. Cell *125*, 1361–1374.

Haigo, S.L., and Bilder, D. (2011). Global tissue revolutions in a morphogenetic movement controlling elongation. Science *331*, 1071–1074.

Kassianidou, E., Brand, C.A., Schwarz, U.S., and Kumar, S. (2017). Geometry and network connectivity govern the mechanics of stress fibers. Proc. Natl. Acad. Sci. USA *114*, 2622–2627.

Klein, F., Striebel, T., Fischer, J., Jiang, Z., Franz, C.M., von Freymann, G., Wegener, M., and Bastmeyer, M. (2010). Elastic fully three-dimensional microstructure scaffolds for cell force measurements. Adv. Mater. 22, 868–871.

Kumar, A., Maitra, A., Sumit, M., Ramaswamy, S., and Shivashankar, G.V. (2014). Actomyosin contractility rotates the cell nucleus. Sci. Rep. 4, 3781.

Labouesse, C., Verkhovsky, A.B., Meister, J.J., Gabella, C., and Vianay, B. (2015). Cell shape dynamics reveal balance of elasticity and contractility in peripheral arcs. Biophys. J. 108, 2437–2447.

Lee, J.P., Kassianidou, E., MacDonald, J.I., Francis, M.B., and Kumar, S. (2016). N-terminal specific conjugation of extracellular matrix proteins to 2-pyridinecarboxaldehyde functionalized polyacrylamide hydrogels. Biomaterials 102, 268–276.

Lieber, A.D., Yehudai-Resheff, S., Barnhart, E.L., Theriot, J.A., and Keren, K. (2013). Membrane tension in rapidly moving cells is determined by cytoskeletal forces. Curr. Biol. 23, 1409–1417.

Lieber, A.D., Schweitzer, Y., Kozlov, M.M., and Keren, K. (2015). Front-to-rear membrane tension gradient in rapidly moving cells. Biophys. J. 108, 1599–1603.

Mertz, A.F., Banerjee, S., Che, Y., German, G.K., Xu, Y., Hyland, C., Marchetti, M.C., Horsley, V., and Dufresne, E.R. (2012). Scaling of traction forces with the size of cohesive cell colonies. Phys. Rev. Lett. 108, 198101.

Nisenholz, N., Rajendran, K., Dang, Q., Chen, H., Kemkemer, R., Krishnan, R., and Zemel, A. (2014). Active mechanics and dynamics of cell spreading on elastic substrates. Soft Matter 10, 7234–7246.

Oakes, P.W., Wagner, E., Brand, C.A., Probst, D., Linke, M., Schwarz, U.S., Glotzer, M., and Gardel, M.L. (2017). Optogenetic control of RhoA reveals zyxin-mediated elasticity of stress fibres. Nat. Commun. 8, 15817.

Owen, L.M., Adhikari, A.S., Patel, M., Grimmer, P., Leijnse, N., Kim, M.C., Notbohm, J., Franck, C., and Dunn, A.R. (2017). A cytoskeletal clutch mediates cellular force transmission in a soft, three-dimensional extracellular matrix. Mol. Biol. Cell 28, 1959–1974.

Palecek, S.P., Loftus, J.C., Ginsberg, M.H., Lauffenburger, D.A., and Horwitz, A.F. (1997). Integrin-ligand binding properties govern cell migration speed through cell-substratum adhesiveness. Nature 385, 537–540.

Pasapera, A.M., Schneider, I.C., Rericha, E., Schlaepfer, D.D., and Waterman, C.M. (2010). Myosin II activity regulates vinculin recruitment to focal adhesions through FAK-mediated paxillin phosphorylation. J. Cell Biol. 188, 877–890.

Pontes, B., Monzo, P., Gole, L., Le Roux, A.L., Kosmalska, A.J., Tam, Z.Y., Luo, W., Kan, S., Viasnoff, V., Roca-Cusachs, P., et al. (2017). Membrane tension controls adhesion positioning at the leading edge of cells. J. Cell Biol. 216, 2959–2977.

Ramirez-San Juan, G.R., Oakes, P.W., and Gardel, M.L. (2017). Contact guidance requires spatial control of leading-edge protrusion. Mol. Biol. Cell 28, 1043–1053.

Raucher, D., and Sheetz, M.P. (2000). Cell spreading and lamellipodial extension rate is regulated by membrane tension. J. Cell Biol. 148, 127–136.

Reinhart-King, C.A., Dembo, M., and Hammer, D.A. (2005). The dynamics and mechanics of endothelial cell spreading. Biophys. J. 89, 676–689.

Rezakhaniha, R., Agianniotis, A., Schrauwen, J.T., Griffa, A., Sage, D., Bouten, C.V., van de Vosse, F.N., Unser, M., and Stergiopulos, N. (2012). Experimental investigation of collagen waviness and orientation in the arterial adventitia using confocal laser scanning microscopy. Biomech. Model. Mechanobiol. 11, 461–473.

Ridley, A.J., Schwartz, M.A., Burridge, K., Firtel, R.A., Ginsberg, M.H., Borisy, G., Parsons, J.T., and Horwitz, A.R. (2003). Cell migration: integrating signals from front to back. Science 302, 1704–1709.

Röttgermann, P.J.F., Alberola, A.P., and Rädler, J.O. (2014). Cellular self-organization on micro-structured surfaces. Soft Matter 10, 2397–2404.

Ruprecht, V., Monzo, P., Ravasio, A., Yue, Z., Makhija, E., Strale, P.O., Gauthier, N., Shivashankar, G.V., Studer, V., Albiges-Rizo, C., and Viasnoff, V. (2017). How cells respond to environmental cues - insights from bio-functionalized substrates. J. Cell Sci. 130, 51–61.

Schwarz, U.S., and Gardel, M.L. (2012). United we stand: integrating the actin cytoskeleton and cell-matrix adhesions in cellular mechanotransduction. J. Cell Sci. 125, 3051–3060.

Shemesh, T., Verkhovsky, A.B., Svitkina, T.M., Bershadsky, A.D., and Kozlov, M.M. (2009). Role of focal adhesions and mechanical stresses in the formation and progression of the lamellum interface. Biophys. J. 97, 1254–1264.

Shemesh, T., Bershadsky, A.D., and Kozlov, M.M. (2012). Physical model for self-organization of actin cytoskeleton and adhesion complexes at the cell front. Biophys. J. 102, 1746–1756.

Shi, Z., Graber, Z.T., Baumgart, T., Stone, H.A., and Cohen, A.E. (2018). Cell Membranes Resist Flow. Cell 175, 1769–1779.e13.

Tabdanov, E.D., Puram, V.V., Win, Z., Alamgir, A., Alford, P.W., and Provenzano, P.P. (2018). Bimodal sensing of guidance cues in mechanically distinct microenvironments. Nat. Commun. 9, 4891.

Théry, M. (2010). Micropatterning as a tool to decipher cell morphogenesis and functions. J. Cell Sci. 123, 4201–4213.

Théry, M., Racine, V., Pépin, A., Piel, M., Chen, Y., Sibarita, J.B., and Bornens, M. (2005). The extracellular matrix guides the orientation of the cell division axis. Nat. Cell Biol. 7, 947–953.

Théry, M., Pépin, A., Dressaire, E., Chen, Y., and Bornens, M. (2006). Cell distribution of stress fibres in response to the geometry of the adhesive environment. Cell Motil. Cytoskeleton 63, 341–355.

Théry, M., Jiménez-Dalmaroni, A., Racine, V., Bornens, M., and Jülicher, F. (2007). Experimental and theoretical study of mitotic spindle orientation. Nature 447, 493–496.

Tojkander, S., Gateva, G., Husain, A., Krishnan, R., and Lappalainen, P. (2015). Generation of contractile actomyosin bundles depends on mechanosensitive actin filament assembly and disassembly. eLife 4, e06126.

Tseng, Q., Wang, I., Duchemin-Pelletier, E., Azioune, A., Carpi, N., Gao, J., Filhol, O., Piel, M., Théry, M., and Balland, M. (2011). A new micropatterning method of soft substrates reveals that different tumorigenic signals can promote or reduce cell contraction levels. Lab Chip 11, 2231–2240.

Wang, W.Y., Pearson, A.T., Kutys, M.L., Choi, C.K., Wozniak, M.A., Baker, B.M., and Chen, C.S. (2018). Extracellular matrix alignment dictates the organization of focal adhesions and directs uniaxial cell migration. APL Bioeng. 2, 046107.

Wolf, K., Wu, Y.I., Liu, Y., Geiger, J., Tam, E., Overall, C., Stack, M.S., and Friedl, P. (2007). Multi-step pericellular proteolysis controls the transition from individual to collective cancer cell invasion. Nat. Cell Biol. 9, 893–904.

Wolf, K., Te Lindert, M., Krause, M., Alexander, S., Te Riet, J., Willis, A.L., Hoffman, R.M., Figdor, C.G., Weiss, S.J., and Friedl, P. (2013). Physical limits of cell migration: control by ECM space and nuclear deformation and tuning by proteolysis and traction force. J. Cell Biol. 201, 1069–1084.

STAR★METHODS

KEY RESOURCES TABLE

REAGENT or RESOURCE	SOURCE	IDENTIFIER
Chemicals, Peptides, and Recombinant Proteins		
PLL(20)-g[3.5]-PEG(2)	Surface Solutions, Switzerland	N/A
Blebbistatin	Sigma	Cat# B0560; CAS# 856925-71-8
Collagen type 1, bovine	Advanced Biomatrix	Cat#5005
40% Acrylamide	Bio-Rad	Cat# 161-0140
2% Bis solution	Bio-Rad	Cat# 161-0142
TEMED (N,N,N',N'-tetramethylethylenediamine	Bio-Rad	Cat# 161-0800; CAS# 110-18-9
Ammounium Persulfate	Bio-Rad	Cat# 161-0700; CAS# 7727-54-0
2PCA-PAA	Lee et al., 2016	N/A
Experimental Models: Cell Lines		
U2OS	ATCC	Cat# HTB96; RRID:CVCL_0042
Recombinant DNA		
Plasmid: pCMV-LifeAct-TagRFP	Ibidi	Cat# 60102
Software and Algorithms		
ImageJ	NIH, Bethesda	N/A
R version 3.4.1 for fitting time constants of spreading and plotting	Vienna, Austria	https://www.R-project.org/
Python 2.7.13 custom scripts for analysis	This paper	N/A
Custom code for Cellular Potts Model	Modified from Albert and Schwarz, 2016a	N/A
GraphPad Prism 7	GraphPad software	https://www.graphpad.com/scientific-software/prism/
CleWin 4.0 for mask design	N/A	Wieweb.com

CONTACT FOR REAGENT AND RESOURCE SHARING

Further information and requests for reagents and analysis should be directed to Sanjay Kumar (skumar@berkeley.edu) and Ulrich S. Schwarz (schwarz@thphys.uni-heidelberg.de).

EXPERIMENTAL MODEL AND SUBJECT DETAILS

293T cells were used to package viral particles of pFUG-RFP-LifeAct and following viral purification, U2OS cells (ATCC HBT-96) were infected at a multiplicity of infection (MOI) of 1.5. U2OS cells expressing RFP-LifeAct were sorted on a DAKO-Cytomation MoFlo High Speed Sorter. Cells were cultured in DMEM with 10% fetal bovine serum (JR scientific), 1% penicillin/strep (Thermo Fischer Scientific) and 1% Non-Essential Amino Acids (Life Technologies).

METHOD DETAILS

Deep-UV based micropattern fabrication

CleWin 4.0 was used to design the rectangular features used in this study, and aBeam technologies (Hayward, CA) printed the chrome quartz photomask. The total fibronectin (FN) area and final pattern area (1200 μm^2) were kept constant for both top and side patterns. Photopatterns were made as previously described (Azioune et al., 2010; Kassianidou et al., 2017). Briefly, glass coverslips were sonicated in 70% ethanol for 10 minutes and air-dried. Coverslips were then plasma treated for 5 minutes. They were then coated with 100 μl of 0.01mg/ml PLL-PEG (Surface Solutions, Switzerland) resuspended in 10 mM HEPES pH = 7.4 for 1 hour. Excess PLL-PEG solution was carefully removed from coverslips which were then air-dried. A drop of water was placed on the photomask and the coverslip was inverted onto the mask (PLL-PEG side touching the mask). Care was taken to remove excess water and

any air bubbles. Coverslips were then exposed to deep UV (UVO cleaner, Jelight, USA) through the photomask. After deep UV incubation, coverslips were carefully removed from the mask by adding water between the coverslip and mask surface and incubated in UltraPure water for at least 30 minutes. Finally, coverslips were incubated with 34.25 μg/ml of FN (EMD Millipore Corporation) in 10 mM HEPES pH = 8.5 for at least 1 hour at 37°C. Patterns were washed 3 times for 5 min in phosphate-buffered saline (PBS) prior to use.

Fluorescence time lapse experiments of cell spreading
6-well plates were laser cut to create a square of 1.5 cm by 1.5 cm. Patterned coverslips were glued at the bottom of these 6-well plates and washed extensively with PBS to ensure removal of any glue trace and no leakage over time. 120,000 U2OS RFP-LifeAct cells were seeded per well. We carefully changed cell media 30 minutes after seeding to remove floating cells. The plate was then placed on an inverted Nikon TI-Eclipse microscope with a motorized stage and an incubator chamber set to 37°C with 5% CO_2. Time-lapse positions were selected, and imaging began at 1 hour 20 minutes after seeding. Images of RFP-LifeAct were taken every 10 minutes for at least 7 hours using a 40x, N.A = 0.75 objective (no binning). We employed the Perfect Focus system to ensure that stress fibers (SFs) remained in focus during spreading. For presentation purposes, the contrast and brightness of fluorescence images were optimized using ImageJ (NIH) (Videos S1 and S5). We conducted five independent experiments and tracked at least 50 cells per experiment. For blebbistatin-treated cell spreading experiments, we treated adherent cells with 3 μM blebbistatin for 1 hour 30 minutes before trypsinization. During trypsinization, cells were also incubated in medium containing blebbistatin. 120,000 cells were seeded on the micropatterns at 2 hours of blebbistatin incubation. Media changes and imaging were performed as described above (Video S3). Cells spread for at least 7 hours in the presence of 3 μM blebbistatin. 3 independent experiments were conducted and at least 50 cells were tracked per experiment. Analysis was performed only on cells which had focused SFs throughout the imaging window and had spread fully on the pattern.

DIC Time Lapse experiments of cell spreading (Figure S1)
Differential Interference Contrast (DIC) imaging of spreading cells on the micropatterns was performed using an inverted Nikon TE2000-E2 microscope equipped with a motorized stage (Prior Scientific), an incubator chamber set at 37°C with 5% CO_2. Cell seeding was performed as described above. Cells were imaged every 45 s for at least 5 hours using a 40x objective. Four independent experiments were conducted and 4 cells were tracked per experiment.

U2OS cells spreading on 2PCA-polyacrylamide gels conjugated with collagen (Figures 7 and S7)
36 kPa 2PCA-PAA gels were fabricated as described previously (Lee et al., 2016). Briefly, 40% acrylamide (BioRad) and 2% bis-acrylamide (BioRad) were combined to a final acrylamide and bis-acrylamide percentage of 15% and 1.2% respectively. The solution was mixed with ammonium persulfate solution (10% in deionized water, final concentration 1.0% w/v), tetramethylethylenediamine (1:1000 v/v) and 2PCA-AA (0.1% mol fraction of acrylamide monomer content). This solution was polymerized between a silanized glass bottom dish (MatTek) and a coverslip treated with hydrophobic solution and allowed to polymerize at room temperature for 15-20 minutes. The coverslip treated with hydrophobic solution was then removed and the gel was briefly rinsed with PBS. 100 μg/ml collagen (bovine Type 1, Advanced Biomatrix) diluted in PBS was incubated on the gels overnight at 37°C and rinsed extensively.

U2OS cells were then seeded onto the gels and allowed to adhere. After 30 minutes, the medium was replaced with CO_2-independent, phenol red-free medium supplemented as described above. Imaging was started 1 hour after seeding. Cells were tracked with a 60x/1.40 oil-immersion objective using DIC every 10 minutes and simultaneously under fluorescence every 20 minutes for at least 6 hours. Cells used in fixation experiments were allowed to spread for 7-8 hours before being fixed in 4% paraformaldehyde for 10 minutes.

To correct for uneven illumination, DIC images were processed by applying a 25-pixel radius Gaussian blur and subtracting this from the original image. A 1-pixel radius median filter was subsequently applied to remove salt and pepper noise. LifeAct fluorescence images were corrected for photobleaching using the Bleach Correction plugin.

Quantification of cell area analysis (Figures 1 and S2)
First, cells were classified based on initial pattern binding position. For the top pattern, we identified 3 positions: right short edge, left short edge, and long edge. Negligible numbers of cells bound to the short regions of matrix surrounding the gap. For the side pattern, cells bound on the short edge, on the top long edge, or the bottom long edge. Due to the observed symmetry between left and right corner binding on top patterns and between top and bottom edge binding on side patterns, these two conditions were treated as equivalent. For this analysis, we used ImageJ (NIH) to threshold images based on RFP-LifeAct signal. As seen in the images in Figure 1, RFP-LifeAct strongly labels the peripheral SFs which we consider to be the cell boundaries. However, the corners of cells are devoid of peripheral SFs, so we used low thresholding to ensure retention of edges. Area measurements based on thresholding were then normalized to 1200 μm^2 (the designed pattern area). As a result of the low thresholding and the constant ruffling, some of our measurements were above 100%. Cells whose area was greater than 0.5 (600 μm^2) in the first image were excluded from the analysis.

SF angle analysis (Figures 2, S3, and S4)

Cell images taken at different time points were merged in a stack and aligned using Template Matching (Tseng et al., 2011). For each time point, the pattern was pruned so that only SFs in the interior of the cell remained. The orientation of the internal SFs was determined using OrientationJ Distribution plugin (Rezakhaniha et al., 2012) in ImageJ (NIH). The structure tensor A for each pixel was calculated using a Gaussian analysis window of size 1 pixel and a cubic spline gradient. From the components A_{ij} of the structure tensor and its eigenvalues λ_{max} and λ_{min}, the directional orientation $1/2\arctan(2(A_{xy}/A_{yy} - A_{xx}))$, the energy $A_{xx} + A_{yy}$ and the coherency $(\lambda_{max} - \lambda_{min})/(\lambda_{max} + \lambda_{min})$ was calculated for each pixel (Rezakhaniha et al., 2012) and a histogram over all pixels was calculated and filtered with a Gaussian kernel of $2°$. Only pixels with an energy larger than 1% of the maximum energy were considered in the histogram aiming at eliminating indistinct image features. In addition, the histogram was weighted by the coherency value, giving anisotropic structures, such as SFs, a larger contribution as compared to flat image regions with uncertain local orientation.

From the cell images, time points were registered in which the cell area adopted one of its characteristic states (see Figure 2 schematics). Depending on the pattern, orientation histograms were calculated for those 2 or 3 characteristic states and 17 temporally equidistant time points in between. Missing orientation histograms were interpolated by calculating the average of the histograms of the surrounding time points. For each of the 19 equidistant time points, orientation histograms were averaged and normalized.

We also compared the resulting orientation histograms with the final fiber orientation distribution at each time point using the Kullback-Leibler (KL) divergence:

$$D(A\,||\,B) = \sum_{i=1}^{N} A(x_i)\log\left(\frac{A(x_i)}{B(x_i)}\right)$$

where N is the number of angular bins.

This quantity determines the difference between distribution A and B by calculating their information loss upon replacing distribution A with B. For equal distributions, the KL divergence is zero. We mostly obtain curves that decrease toward zero, when comparing the distributions to the final configuration as a function of time, which indicates that the SF orientation gradually approaches its final orientation distribution (Figure S3).

Segmentation of SFs

We used the plugin Filament Sensor v0.1.7 to segment out single SFs from the fluorescence images, as shown in Figure 2 (Eltzner et al., 2015). Images were filtered with a Gaussian filter of width 0.5 pixels and a subsequent Laplace filter of width 1 pixel. Moreover, a directed Gaussian filter of width 1 pixel was applied and only filaments starting from a minimal length of 20 pixel were considered.

SF distance analysis (Figures 4 and S4)

The fluorescence intensity of the cell image along a line both close and parallel to the boundary of the pattern where new FAs are created was determined using ImageJ (NIH) and averaged over time. The resulting averaged intensity distribution was spatially filtered by means of a Gaussian kernel of width 0.32 μm and the distances between adjacent intensity maxima were determined.

SF lifetime analysis (Figures 6 and S6)

Cell images were first aligned using Template Matching (Tseng et al., 2011). A region of interest (ROI) was drawn over the SF using Polygon selection in ImageJ (NIH). SFs were chosen to ensure that they would not migrate outside of the ROI prior to their disintegration. The fluorescent intensity of SFs within the ROI was then determined using Plot Z axis profile in ImageJ (NIH) and plotted as a function of time. An exponential curve was fit to the data to determine the SF half-life (τ) in seconds using a custom Python script. Multiple ROIs were analyzed per cell. The distance of the SF of interest from the spreading edge was determined from the point of FA (binding of SF to the FN line). If the SF was at a diagonal position due to the presence of 2 lamellipodial structures (one on each 1D FN line), the distance to the lamellipodium was determined based on the leading lamellipodial structure. At least 15 cells were analyzed per pattern (side and top pattern). Plots, fits and correlation statistics were determined using GraphPad Prism 7.

Model Description (Figures 1, 3, and 5)

We extend our previously developed 2D cellular Potts model (CPM) to show that the distribution of SFs is mainly dictated by the pattern geometry and the associated spreading process. The CPM is implemented on a 2D square lattice so that each lattice site can either belong to the cell or the surroundings. Additionally, lattice sites can be defined as adhesive, which makes it possible to implement underlying patterns. The Metropolis algorithm is used to simulate cell spreading by randomly trying to flip a lattice site at the cell periphery. The acceptance probability is calculated from the following energy functional:

$$H = \sigma A + \lambda_s l + \sum_{arci} \frac{EA}{2L_{0,i}}(L_i - L_{0,i})^2 - \frac{E_0}{A_{ref} + A_{ad}}A_{ad} \tag{1}$$

where the first term accounts for surface tension σ and hence scales linearly with the cell area A. The second term is the contribution due to simple line tension which is proportional to the cell perimeter l. In addition to this simple line tension, we account for an extra elastic line tension present in free arcs, seen in the third term, and EA is the associated elastic modulus. The last term considers the

adhesion energy due to the adhesive pattern where A_{ad} is the adhered area. Further details of the model can be found in our previous work (Albert and Schwarz, 2014). The implementation of SFs is new to our model and originates in the idea that SFs are formed parallel to the advancing front in a periodic process. Hence, we integrate a rule that SFs are formed between two points that previously supported an arc spanning a non-adhesive area. However, a minimum distance is introduced that corresponds to the experimentally observed average distance between two adjacent SFs (2.5 μm). Before defining a specific SF, the distance to the previously introduced SF is checked and the SF is only accepted if at least this minimum distance is fulfilled at the faster spreading side. Furthermore, SFs are always introduced as straight lines but are only shown if completely covered by the cell body. Although SFs might be remodeled in the living cell, the model does not allow for changes after the fibers have been put down. All simulations were averaged over 100 spreading events for each binding position on each pattern. The distributions from the simulations were constructed taking CPM data from different regions of the pattern according to the benchmark times introduced earlier (Figure 2). Early SFs formed during the initial spreading phase (t_1) are highlighted in light blue and later SFs formed during t_2 and t_3 are highlighted in darker shades of blue.

Fit of model parameters to experiments

We use a minimization procedure based on the Nelder-Mead algorithm (as implemented in SciPy) to fit the simulation parameters to the experimentally obtained data. As a quantitative comparison, we use the time evolution of the central point on the invaginated arc. Therefore, a distance measure can be calculated by evaluating the mean squared deviation between the two corresponding trajectories. The parameter fit is accomplished through the following steps: First, a suitable set of initial parameters is found by a coarse scan of the relevant parameter ranges. Then, the optimization procedure is started, which runs the CPM with the given initial parameters and uses the Nelder-Mead simplex algorithm to determine the next set of parameters according to the minimization of the distance measure. Finally, once the algorithm converges to the optimal parameter set, it stops. In principle, an additional parameter also scales the time of the simulation. However, this value must be fixed across all simulations to allow meaningful comparison of the extracted parameter values.

In order to estimate the radius of curvature R and spanning distance d of the cells on the micropatterns, circles were placed manually along the brightest region of the corresponding stress fiber. Both parameters were determined based on these circles. See Figure S2 for values.

QUANTIFICATION AND STATISTICAL ANALYSIS

Statistical comparisons were carried out using GraphPad Prism 7, R version 3.4.1 and Python. Non parametric Mann-Whitney tests were carried out when two cases were compared. Differences were considered to be significant when calculated p values were below 0.05. Details on sample size are found in the figure legends. Statistical analysis p values are found in Table S1 and in the appropriate figure legends. All box and whisker plots are further explained in the figure legends.